American Welding Society®

SUPPLEMENT TO THE *WELDING JOURNAL*, NOVEMBER 2022
Sponsored by the American Welding Society

WELDING RESEARCH

Thin Molten Pool Behaviors in Blue Laser Microjoining

Marangoni stress determines the stability of the thin molten pool in blue laser microjoining

BY D. WU, J. SUN, Z. LI, J. HUANG, AND K. FENG

Abstract

Thin copper materials are difficult to weld using infrared lasers (IR) due to their low energy absorption. A blue laser with a wavelength of 450 nm strongly increases energy absorption and successfully realized the microjoining of a copper material with a thickness of 0.1 mm. The dynamic behaviors of a thin molten pool were investigated by a numerical simulation using a new blue laser heat source model. At both the top and bottom surfaces of the thin molten pool, the liquid metal flowed outward under the driving of Marangoni stress. The stability of the thin molten pool was studied, showing that Marangoni stress promoted the melt-through of the thin molten pool, while the viscous resistant stress, buoyant force, and surface tension pressure had minor influences on it. The Peclet and Marangoni numbers were adopted to predict the stability of the thin molten pool.

Keywords

- Blue Laser
- Microjoining
- Energy Absorption
- Thin Molten Pool
- Copper Material

https://doi.org/10.29391/2022.101.021

Introduction

With the increasing demand for electric vehicles (Ref. 1), the usage of pure copper and copper alloys has also increased due to their high thermal and electric conductivity (Ref. 2). Therefore, microjoining of copper materials is required (Ref. 3). Arc energy density is low, making the arc welding processes difficult to realize the high efficient microjoining of copper materials that have a small heat-affected zone (HAZ). Laser welding processes have the advantages of high energy density, precision, efficiency, and flexibility (Ref. 4); however, copper materials have very low absorptivity for commonly used infrared (IR) lasers with near 1000 nm wavelengths (Ref. 5). More than 90% of the laser power will be reflected if an IR laser irradiates on a copper surface (Ref. 6). Even though using laser power modulation (Ref. 7), a wobbling laser (Ref. 8), and the preheating method (Ref. 9) can improve the IR laser beam's absorptivity in keyhole welding of thick copper plates, weld defects such as spatter and porosity can't be effectively eliminated. Microjoining of copper materials by an IR laser is impossible.

Instead of using an IR laser, a laser with a wavelength of 450 nm strongly increases the absorptivity of copper materials (Ref. 10). Fujio et al. (Ref. 11) showed that at a wavelength of 450 nm, copper has an absorption rate about six times higher than that of the IR's region. Hummel et al. (Ref. 12) measured the laser absorption in blue laser welding of copper alloys with integrating spheres; the measurements indicated that with blue laser absorptivity varies between 72.6 and 76.6% on $CuSn_6$ alloy, and between 69.8 and 83.1% on Cu-ETP. Britten et al. (Ref. 13) proposed that the surface condition of a copper sheet has a minor influence on blue laser absorption, and consistently high weld seam quality was achieved with etched, oxidized, and polished surface conditions. Morimoto et al. (Ref. 14) suggested that for a blue laser, the absorption rate of copper didn't depend on temperature. Due to their

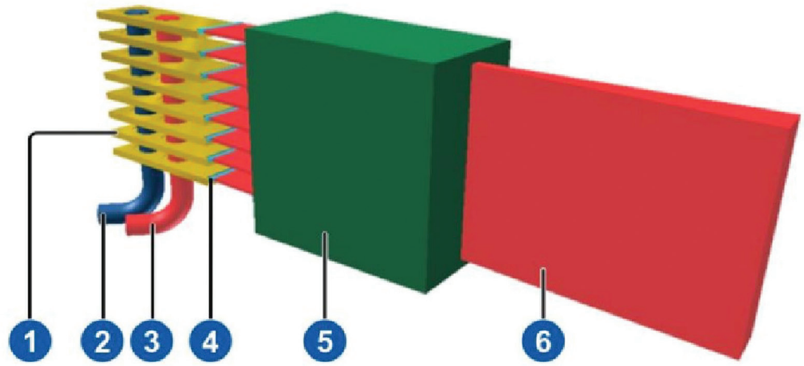

Fig. 1 — Concept of power scaling with diode bars for LDMblue 1000-100.

high and stable absorptivity, copper plates can be joined by a blue laser with low laser power and high efficiency and quality. Spatter and porosity can be successfully eliminated in blue laser keyhole welding (Ref. 15). Microjoining of copper materials by a blue laser is also possible. Pelaprat et al. (Ref. 16) used a blue laser to join 70-µm thick copper materials with a laser power of 130 W. Zediker et al. (Ref. 17) also adopted a blue laser to join multilayer super-thin copper foils.

In a blue laser microjoining process, the copper materials are very thin. As a result, a molten pool with a large length and a low height (thin molten pool) is formed. The molten metal flow patterns inside a thin molten pool, and

Table 1 — Chemical Compositions (wt-%) of 304 Stainless Steel Used in the Experiment

C	Mn	Si	P	S	Ni	Cr	Cu	Mo	Co	N	Fe
0.043	0.95	0.41	0.031	0.005	8.03	18.09	0.023	0.004	0.237	0.054	Bal.

Table 2 — Thermophysical Properties of T2 Copper, Pure Titanium, and 304 Stainless Steel

Nomenclature	Copper	Titanium	304
Melting point (K)	1357.85	1941	1727
Latent heat of fusion (J·kg^{-1})	2.087×10^{5}	4.354×10^{5}	2.47×10^{5}
Coefficient of thermal expansion (K^{-1})	1.85×10^{-5}	1.1×10^{-5}	1.42×10^{-5}
Surface tension (N·m^{-1})	1.304	1.525	1.632
Surface tension gradient (N·m^{-1}·K^{-1})	-2.84×10^{-4}	-2.8×10^{-4}	0.9×10^{-4}

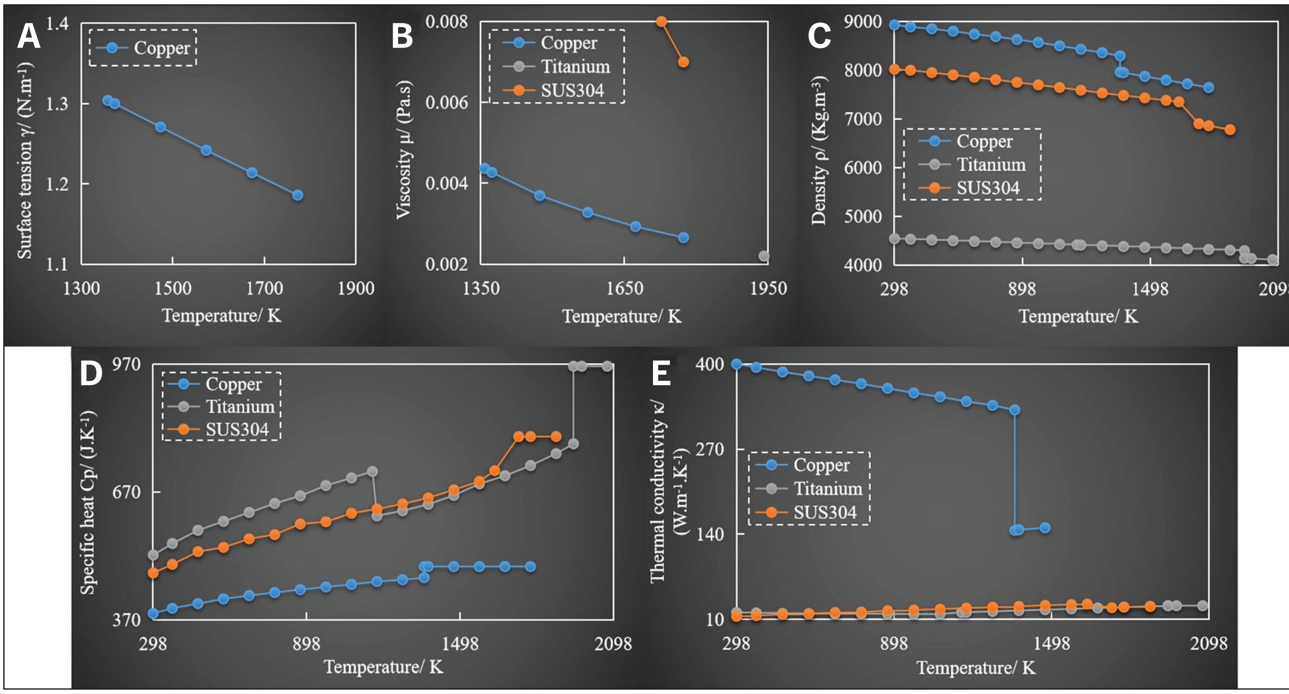

Fig. 2 — Thermophysical material properties of T2 copper, pure titanium, and SUS304 stainless steel. A — Surface tension; B — viscosity; C — density; D — specific heat; E — thermal conductivity.

the stability mechanism of a thin molten pool have never been investigated.

In this study, a blue laser was adopted to realize the microjoining of copper material with a thickness of 0.1 mm. A new blue laser heat source model was developed in a numerical simulation to investigate the dynamic behaviors of a thin molten pool. The influences of material properties on the thin molten pool behaviors will be discussed. The stability mechanism of the thin molten pool will also be revealed.

Experiment Procedures

The blue diode laser system LDMblue 1000-100 with a maximum power of 1000 W, a wavelength of 450 nm, and a focus spot diameter of 1.0 mm was used. As shown in Fig. 1, this blue diode laser system used laser bars to mount and electrically connect. The diode laser bars were supplied with current and water. The direct current applied excited the semiconductor material of the diode laser chip to lase. The cooling water absorbed the heat generated by the emitting laser beam. To focus the diode laser beam that was emitted, a microrod lens close to the diode laser component in the fast axis (perpendicular to the emitting plane) was used first to collimate the beam. As the beam continued its journey, divergence was collimated in the slow axis direction (parallel to the emitting plane) using a cylindrical lens. Subsequent focusing optics then focused this twice-collimated laser beam onto a small processing spot.

The microjoining experiments were performed under a laser power of 180 W with a defocused distance of 0 mm and a travel speed of 2 m.min^{-1}. Pure argon gas was used as the shielding gas with a flow rate of 25 L·min^{-1}. T2 copper foil with a thickness of 0.1 mm was adopted as the base metal. T2 copper is the equivalent to electrolytic tough pitch (ETP) copper and is 99.9 wt-% Cu with 0.02 to 0.04 wt-% oxygen. The blue laser microjoining experiments of pure titanium and 304 stainless steel foils with thicknesses of 0.1 mm were also carried out to investigate the influences of material properties on molten pool behaviors. The thermophysical material properties of pure copper and titanium and 304 stainless steel can be seen in Ref. 18. The surface tensions of pure copper and titanium were only temperature dependant, while the surface tension of 304 stainless steel was considered as a function of the temperature and sulfur active element. The chemical composition (wt-%) of the 304 stainless steel used in the experiment can be seen in Table 1. The detailed thermophysical material properties can be seen in Fig. 2 and Table 2. Following the microjoining process, the beads were cut, mounted, and polished. The copper sample was etched using a reagent with 5-g ferric chloride, 50-mL hydrochloric acid, and 100-mL water, and the bead geometry was observed using an optical microscope.

Numerical Model of Blue Laser Welding

In numerical simulations of the molten pool in blue laser welding, the liquid metal is considered incompressible Newtonian fluid, and the flow is laminar (Ref. 19). The simulation is based on the numerical solution of mass, momentum, and energy conservation equations, and the volume of fluid (VOF) equation is adopted to track the free fluid surface (Ref. 20).

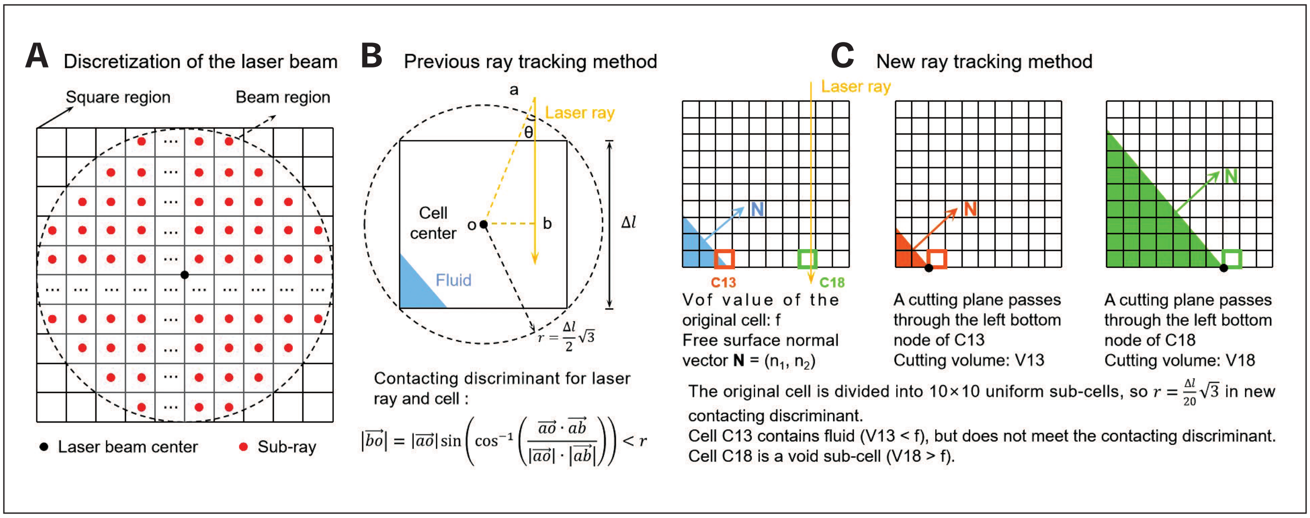

Fig. 3 — A — Discretization of the laser beam; B — previous ray tracking method; C — new ray tracking method.

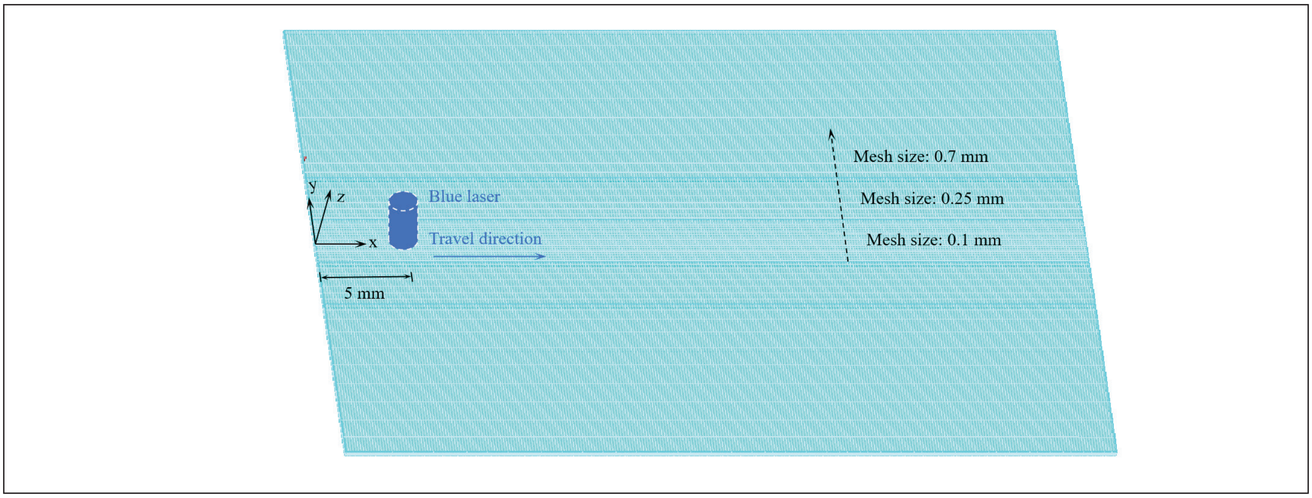

Fig. 4 — Computation domain and mesh size.

Governing Equations

The mass conservation equation is

$$\frac{\partial \rho}{\partial t} + \nabla \cdot (\rho \boldsymbol{v}) = 0 \qquad (1)$$

where ρ is fluid density, *t* is time, and v is a velocity vector.

The momentum conservation equation is

$$\frac{\partial (\rho \boldsymbol{v})}{\partial t} + \nabla \cdot (\rho \boldsymbol{v}\boldsymbol{v}) = -\nabla P + \nabla \cdot \boldsymbol{\tau} + \rho g \qquad (2)$$

where *P* is pressure, τ is a viscosity stress tensor, and *g* is gravity.

The energy conservation equation is

$$\frac{\partial (\rho h)}{\partial t} + \nabla \cdot (\rho \boldsymbol{v} h) = \nabla \cdot (k \nabla T) \qquad (3)$$

where *h* is enthalpy, *k* is thermal conductivity, and *T* is temperature.

The VOF equation is

$$\frac{\partial F}{\partial t} + \nabla \cdot (\rho \boldsymbol{v} F) = 0 \qquad (4)$$

where *F* is the volume fraction of the fluid in a cell. The TruVOF method (Ref. 21) is adopted in FLOW-3D® to reduce the cumulative volume error.

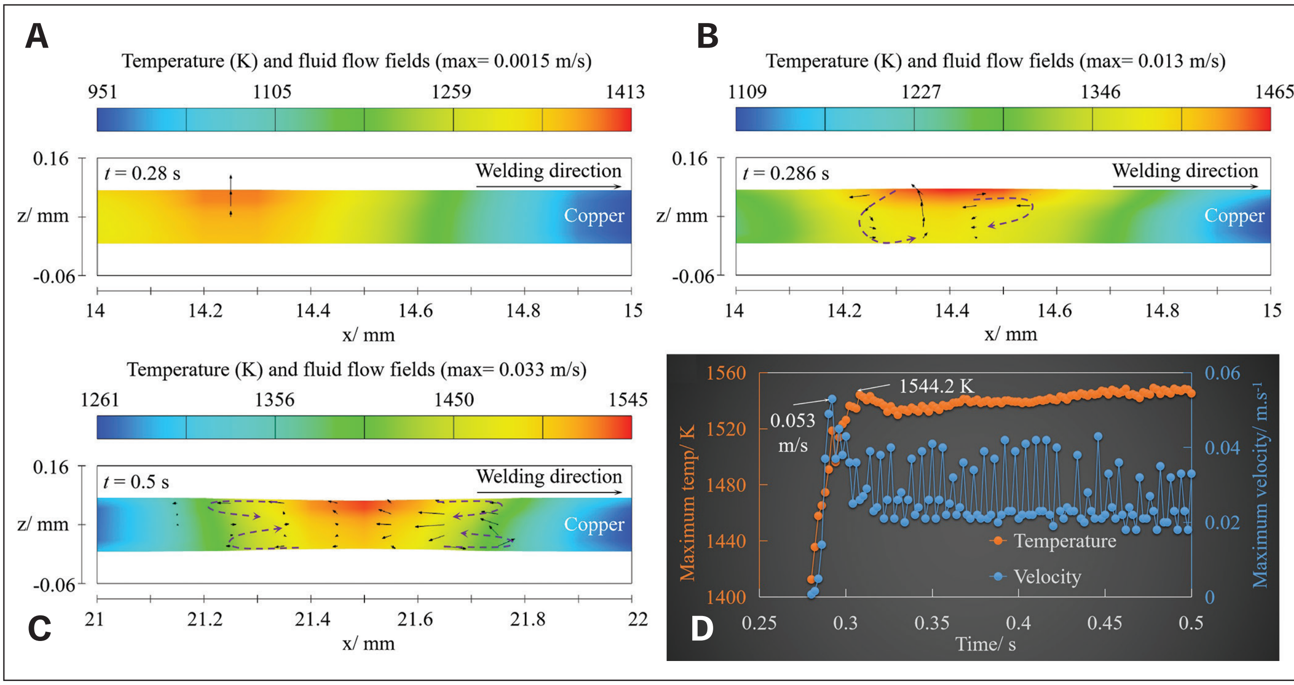

Fig. 5 — Temperature (K) and fluid flow fields in the y = 0 cross section in blue laser microjoining of T2 copper: A — 0.28 s; B — 0.286 s; C — 0.5 s; D — maximum molten temperature and velocity vs. time.

Blue Laser Heat Source Model

At the focus plane, bundles of rays with a Gaussian-like axisymmetric distribution of energy were defined to approximate a real blue laser beam. A square region with a length of 1.0 mm at the focus plane was divided into uniform 50 × 50 sub-cells. The initial point of each ray is predefined as the center of each sub-cell, and the direction vector is (0, 0, −1), as shown in Fig. 3A. The energy of each ray can be expressed as follows:

$$e_{(x,y,z_0)} = \frac{P_b}{\pi r_0^2} exp\left(-\frac{x^2+y^2}{r_0^2}\right) \times A_{sub} \quad (5)$$

where P_b is blue laser power, r_o is the laser beam radius at the focus plane, z_o is the coordinate of the focus plane in the Z direction, x, y are the distances between the sub-cell center and the laser beam center in the X, Y directions, and A_{sub} is the sub-cell area.

When a laser ray contacts with a cell containing a free surface, 63, 44.8 (Ref. 22), and 54% (Ref. 23) values of the ray energy are absorbed by the cell in blue laser microjoining of copper, titanium, and stainless steel, respectively. In this study, a new ray tracking method was adopted. For simplicity, a 2D case is used to describe the improvement of this new ray tracking method. The contacting discriminant for a ray and a cell containing a free surface is that the distance between the cell center and the ray is smaller than $\sqrt{3}\Delta l/2$ (Δl is the cell size). As shown in Fig. 3B, a cell with minimal fluid meets this contacting discriminant. In our previous ray tracking method, this cell absorbed the ray energy (Ref. 24). In our new ray tracking method, to improve calculation accuracy, the cell containing a free surface was divided into 10 × 10 uniform sub-cells in the horizontal and vertical directions, as shown in Fig. 3C. A void sub-cell discriminant was developed: a cutting plane with surface normal vector $\boldsymbol{N}$ passed through the left bottom node of a sub-cell. If the cutting volume was smaller than the VOF value of the original cell, the sub-cell contained fluid; otherwise, this sub-cell was void. Based on the contacting discriminant and void sub-cell discriminant, the ray (yellow arrows in Fig. 3B, C) without actual interactions with the minimal fluid, which is inaccurately captured in the original large cell, will not be captured by the refined sub-cells. As shown in Fig. 3C, sub-cell C13 contained fluid, but did not meet the contacting discriminant; sub-cell C18 met the contacting discriminant, but it was a void sub-cell; therefore, the ray was not captured by these two sub-cells.

Computation Domain and Boundary Conditions

The computation domain with a dimension of 30 × 20 × 0.22 mm was used in the simulation, as shown in Fig. 4. The mesh sizes were 0.1 mm in the x direction and 0.02 mm in the z direction. A nonuniform mesh system was used in the y direction: In the central region, a finer mesh with a size of 0.1 mm was used; from the central region to the outside region, the mesh size gradually increased, and a coarser mesh with a size of 0.7 mm was used in the outside region. The blue laser beam traveled along the x direction, and its start point was (5 mm, 0 mm).

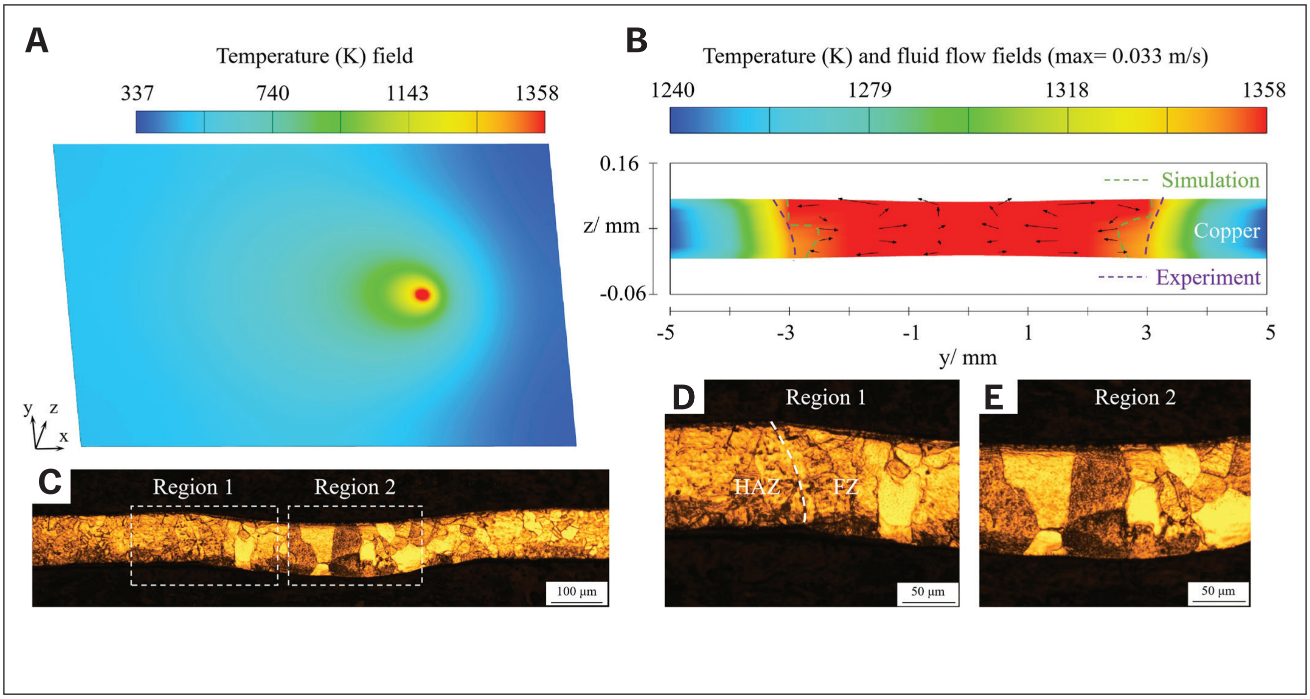

Fig. 6 — Blue laser microjoining of T2 copper: A — Numerical temperature field at the top view at t = 0.5 s; B — temperature (K) and fluid flow fields in the x = 21.45 mm cross section at t = 0.5 s; C — experimental weld joint; D — microstructure in Region 1; E — microstructure in Region 2.

Blue laser heat flux, heat conduction, and radiation were applied on the energy boundary condition of the top free surface:

$$k\frac{\partial T}{\partial \boldsymbol{n}} = 0.63\frac{P_b}{\pi r_0^2}exp\left(-\frac{x^2+y^2}{r_0^2}\right) - h_c\,(T-T_0)\; - \sigma\varepsilon(T^4 - T_0^4) \quad (6)$$

where $\boldsymbol{n}$ is a surface normal vector, h_c is the heat transfer coefficient, T_0 is the ambient temperature, σ is the Stefan-Boltzmann constant, and ε is surface emissivity.

Only heat conduction and radiation were considered on the energy boundary conditions of the left, right, front, and back boundaries and the bottom free surface:

$$-k\frac{\partial T}{\partial \boldsymbol{n}} = -h_c\,(T-T_0)\; - \sigma\varepsilon(T^4 - T_0^4) \quad (7)$$

The pressure balances of the top and bottom free surfaces are expressed as follows:

$$-P + 2\mu\frac{\partial \boldsymbol{v_n}}{\partial \boldsymbol{n}} = -\frac{\gamma}{R} \quad (8)$$

where μ is fluid viscosity, $\boldsymbol{v_n}$ is a normal velocity vector, γ is the surface tension of the fluid, and R is the radius of the surface curvature.

Marangoni stress caused by temperature gradient was applied on both the top and bottom free surfaces in the tangential direction:

$$-\mu\frac{\partial \boldsymbol{v_t}}{\partial \boldsymbol{n}} = \frac{\partial \gamma}{\partial T}\frac{\partial T}{\partial \boldsymbol{S}} \quad (9)$$

where v_t is a tangential velocity vector, $\boldsymbol{S}$ is a tangential vector, and ∂γ/∂T is the surface tension gradient.

In the simulation, the thermophysical material properties of pure copper and titanium, and 304 stainless steel were adopted, and the material compositions in the simulation and experiment were consistent. The surface tension gradients of pure copper and titanium were negative. The sulfur content of the 304 stainless steel was 50 ppm. The surface tension and surface tension gradient of 304 stainless steel at 1973 K were calculated based on Equations 10 and 11 (Refs. 18, 25), and their values were 1.632 $N.m^{-1}$ and 0.9×10^{-4} N.m-1.K^{-1}, respectively.

$$\gamma_{1973} = 1.15 - 0.0909\;\ln\,(\%S) \quad (10)$$

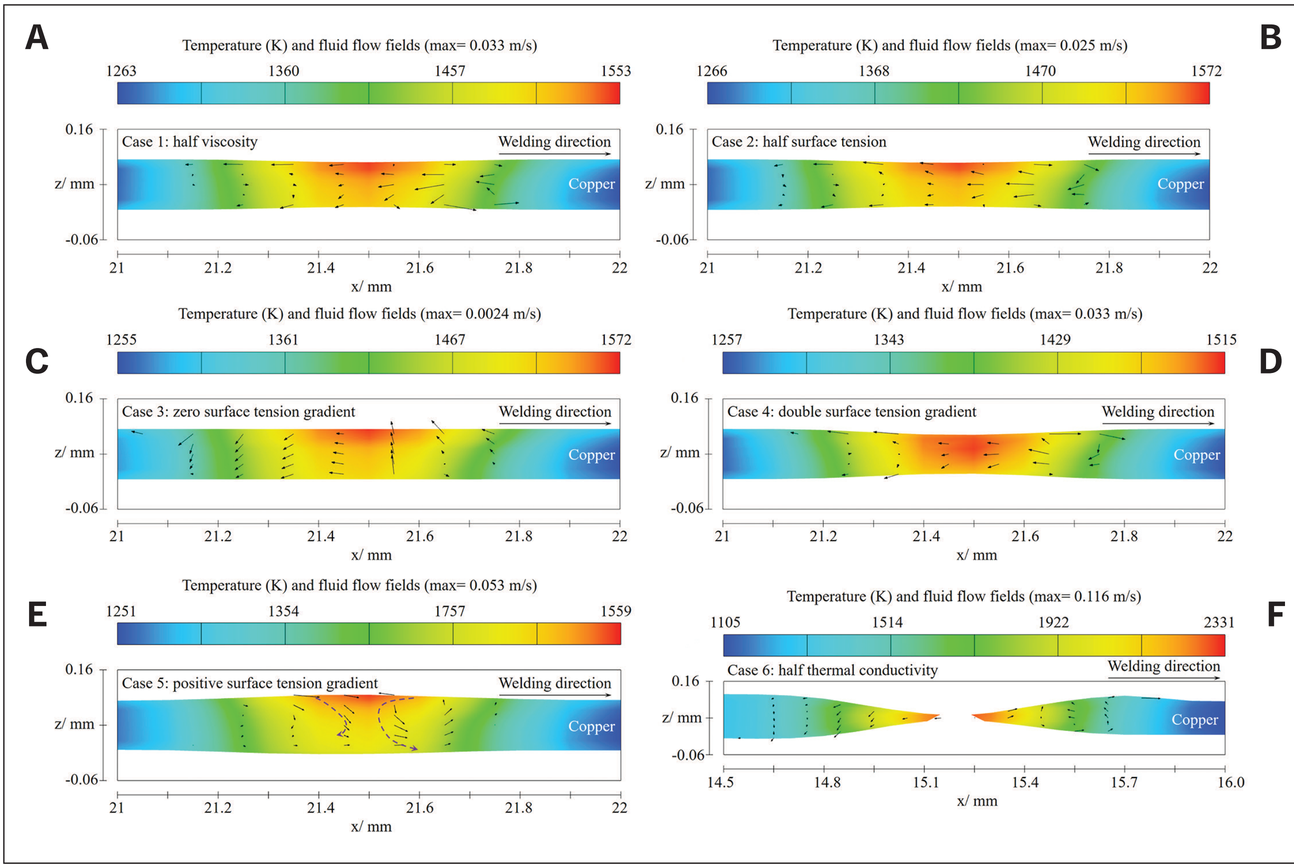

Fig. 7 — Temperature (K) and fluid flow fields in the y = 0 cross section at t = 0.5 s in blue laser microjoining of T2 copper: A — Case 1 with half viscosity; B — Case 2 with half surface tension; C — Case 3 with zero surface tension gradient; D — Case 4 with double surface tension gradient; E — Case 5 with positive surface tension gradient; F — Case 6 with half thermal conductivity.

$$\left(\frac{\partial \gamma}{\partial T}\right)_{1973} = \left(1.51 + 0.268\ \ln\left(\%\mathrm{S}\right)\right) \times 10^{-3} \quad (11)$$

where %S is the weight percentage of sulfur.

The temperature and sulfur content-dependant surface tension of 304 stainless steel can be calculated as follows:

$$\gamma = \gamma_{1973} + \left(\frac{\partial \gamma}{\partial T}\right)_{1973} (T - 1973) \quad (12)$$

Results

Thin Molten Pool Behaviors in Microjoining of Copper

As shown in Fig. 5A, C, in the $y = 0$ cross section, at $t =$ 0.28 s, the copper started to melt, and a small molten pool was formed at the top part. The molten flow was very weak, and the maximum velocity was only 0.0015 m/s. At $t =$ 0.286 s, a penetrated molten pool was generated. As the surface tension gradient was negative, at the top surface, the molten metal flowed outward from the pool center to the pool edge under the driving of Marangoni stress (Ref. 26) and then flowed downward to the bottom surface. When the molten pool reached the quasi-steady state, at $t = 0.5$ s, at both the top and bottom surfaces, the molten metal flowed outward with a maximum velocity of 0.033 m/s. The convective patterns were not symmetric in the $y = 0$ cross section. Both the top and bottom surfaces were slightly deformed. The molten height was only about 0.1 mm while the length was about 0.619 mm.

The maximum molten temperature and velocity are presented in Fig. 5D. The maximum molten temperature rapidly increased to 1544.2 K with an average increasing rate of 4700 K/s and then oscillated around a mean value of 1541 K. The maximum molten velocity rapidly increased to 0.053 m/s and then oscillated around a mean value of 0.028 m/s.

As shown in Fig. 6A, the values of the molten width and length were close and much larger than the molten height (about 0.1 mm), so a thin molten pool formed in the quasi-steady state. As shown in Fig. 6B and C, in the $x = 21.45$ mm cross section at $t = 0.5$ s, the molten metal flowed outward

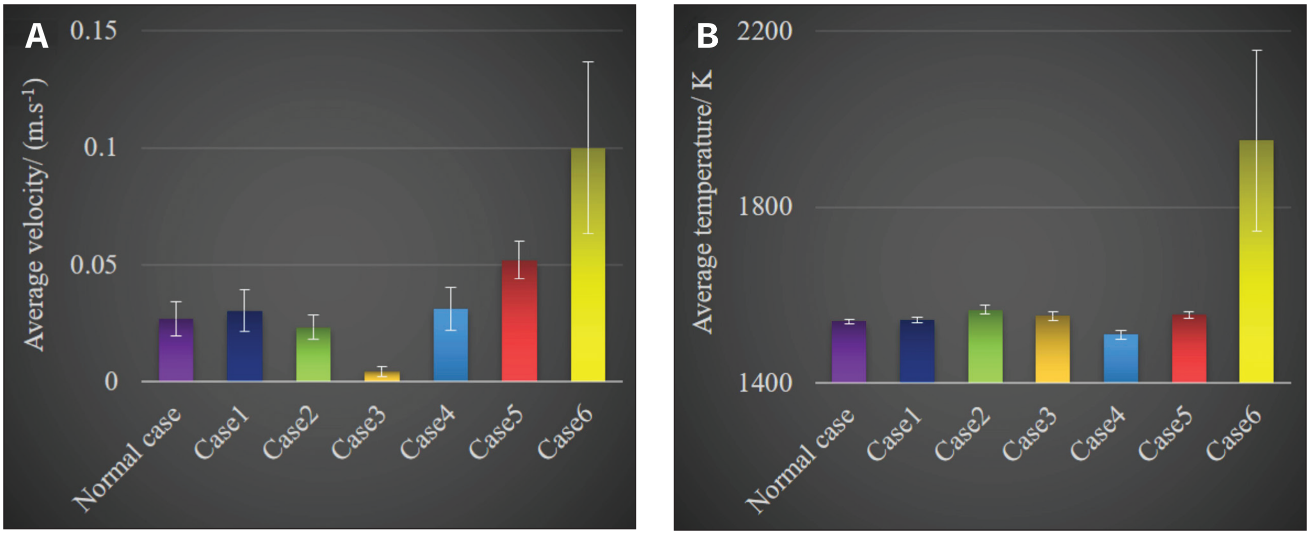

Fig. 8 — Comparisons of different cases: A — Average velocity; B — average temperature.

at both the top and bottom surfaces, and the convective patterns were almost symmetric. The calculated weld widths at the top and bottom surfaces were 0.608 and 0.537 mm, respectively. The experimental weld widths at the top and bottom surfaces were 0.651 and 0.588 mm, respectively; the weld depth appeared to be similar to the original foil thickness, and the weld apparently sagged due to joining. The calculated weld interface did not agree well with the experimental result, which may have been caused by the deformation of the copper foil during the experiment. It can be clearly seen from Fig. 6D and E that the fusion zone (FZ) of the copper joint had grains larger than those in the HAZ.

Table 3 — Condition, Maximum Temperature, and Velocity in Different Cases

Case	Condition	Maximum Velocity ($m \cdot s^{-1}$)	Maximum Temperature (K)
Normal case	Pure copper	0.028	1541
Case 1	Pure copper with half viscosity	0.030	1544
Case 2	Pure copper with half surface tension	0.023	1567
Case 3	Pure copper with zero surface tension gradient	0.0046	1553
Case 4	Pure copper with double surface tension gradient	0.031	1511
Case 5	Pure copper with a positive surface tension gradient	0.052	1555
Case 6	Pure copper with half thermal conductivity	0.10	1952

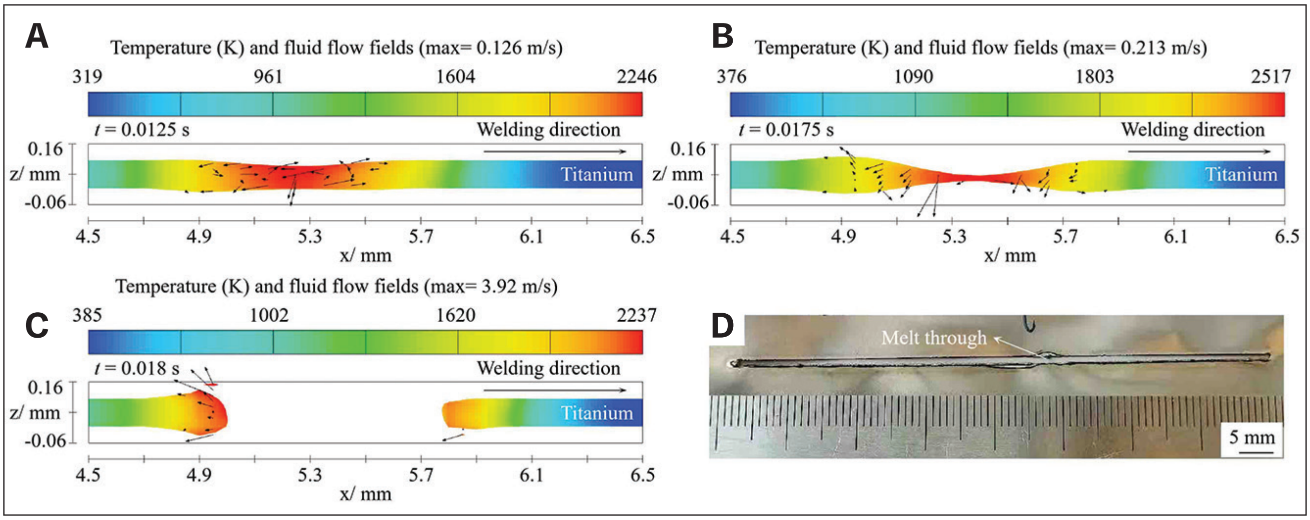

Fig. 9 — Temperature (K) and fluid flow fields in the y = 0 cross section in blue laser microjoining of pure titanium: A — 0.0125 s; B — 0.0175 s; C — 0.018 s; D — experiment result.

Influence of Material Properties on Heat and Mass Transfer in the Thin Molten Pool

As shown in Table 3, different cases were carried out to investigate the influence of material properties on heat and mass transfer in the thin molten pool. The blue laser microjoining of T2 copper with actual material properties was defined as "normal case" (Figs. 5 and 6). A new simulation with half viscosity was restarted from the normal case at $t = 0.3$ s (Case 1 and Fig. 7A). In the $y = 0$ cross section, the maximum molten temperature was 1553 K, and the maximum velocity was 0.033 m/s at $t = 0.5$ s. The molten metal flowed outward at both the top and bottom surfaces. A new simulation with half surface tension was restarted from the normal case at $t = 0.3$ s (Case 2 and Fig. 7B). In the $y = 0$ cross section, the maximum molten temperature was 1572 K, and the maximum velocity was 0.025 m/s at $t = 0.5$ s. In keyhole laser welding, the surface tension is the main resistant force for keyhole formation (Ref. 27), and a keyhole is easy to form in keyhole laser welding of a material with low surface tension (Ref. 28). However, in blue laser microjoining of a thin copper material with half surface tension, the convective patterns inside the molten pool are unchanged and the surface deformation is still small at $t = 0.5$ s. The convective patterns inside the molten pool are unchanged. A new simulation with zero surface tension gradient was restarted from the normal case at $t = 0.3$ s (Case 3 and Fig. 7C). In the $y = 0$ cross section, the maximum molten temperature was 1572 K, and the maximum velocity was only 0.0024 m/s at $t = 0.5$ s. The molten metal flowed downward in the left part and flowed upward in the right part under the driving of the buoyant force. A new simulation with double surface tension gradient was restarted from the normal case at $t = 0.3$ s (Case 4 and Fig. 7D). In the $y = 0$ cross section, the maximum molten temperature was 1515 K, and the maximum velocity was 0.033 m/s at $t = 0.5$ s. The convective patterns inside the molten pool were unchanged. A new simulation with a positive surface tension gradient was restarted from the normal case at $t = 0.3$ s (Case 5 and Fig. 7E). In the $y = 0$ cross section, the maximum molten temperature was 1559 K, and the maximum velocity was 0.053 m/s at $t = 0.5$ s. At the top surface, the molten metal flowed inward from the pool edge to pool center under the driving of Marangoni stress (Ref. 26) and then flowed downward to the bottom surface. A new simulation with half thermal conductivity was restarted from the normal case at $t = 0.3$ s (Case 6 and Fig. 7F). In the $y = 0$ cross section, the maximum molten temperature was 2331 K, and the maximum velocity was 0.116 m/s at $t = 0.3105$ s. The molten pool melts through.

As shown in Fig. 8 and Table 3, with smaller viscous resistant stress, the average maximum molten velocity increased to 0.030 m/s while the average maximum molten temperature (1544 K) was almost unchanged. With half surface tension, the average maximum molten velocity decreased to 0.023 m/s while the average maximum molten temperature increased to 1567 K. With zero surface tension gradient, the average maximum molten velocity decreased to 0.0046 m/s, while the average maximum molten temperature increased to 1553 K. With double surface tension gradient, the average maximum molten velocity increased to 0.031 m/s, while the average maximum molten temperature decreased to 1511 K. With a positive surface tension gradient, the average maximum molten velocity increased to 0.052 m/s and the average maximum molten temperature increased to 1555 K. With half thermal conductivity, the average maximum molten velocity increased to 0.10 m/s and the average maximum molten temperature increased to 1952 K.

In blue laser microjoining of pure titanium, as shown in Fig. 9, in the $y = 0$ cross section, at $t = 0.0125$ s, the molten metal flowed outward at both the top and bottom surfaces. At $t = 0.0175$ s, both the top and bottom surfaces were seriously deformed with a maximum molten temperature of 2517 K and a maximum velocity of 0.213 m/s. The molten metal flowed-backward from the pool center to the pool edge under the driving of Marangoni stress; at the pool center, the molten pool became very thin, and melted through at $t = 0.018$ s.

As the sulfur content was 50 ppm, the surface tension gradient of 304 stainless steel was positive. In blue laser

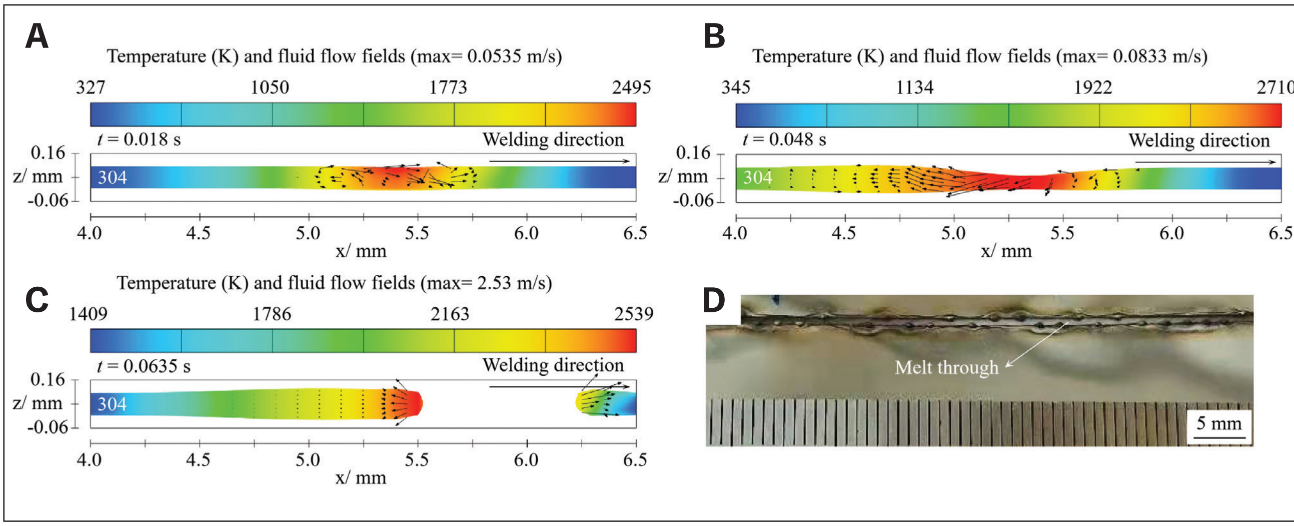

Fig. 10 — Temperature (K) and fluid flow fields in the y = 0 cross section in blue laser microjoining of SUS304 stainless steel: A — 0.018 s; B — 0.048 s; C — 0.0635 s; D — experiment result.

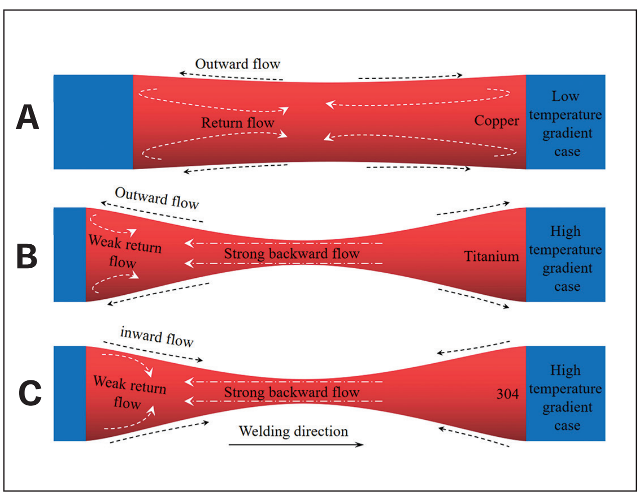

Fig. 11 — Molten pool convection in blue laser microjoining: A — T2 copper; B — pure titanium; C — SUS304 stainless steel.

microjoining of 304 stainless steel, as shown in Fig. 10, in the $y = 0$ cross section at $t = 0.018$ s, the molten metal flowed inward from the pool edge to the pool center under the driving of Marangoni stress at both the top and bottom surfaces with a maximum molten temperature of 2495 K and a maximum velocity of 0.0535 m/s. At $t = 0.048$ s, the molten metal flowed strongly backward with a maximum velocity of 0.0833 m/s, and the molten pool was seriously deformed. At $t = 0.0635$ s, the molten pool melted through. With the same laser energy input, the total energy absorbed by the molten pool was slightly lower, while the melt-through more easily occurred in blue laser microjoining of pure titanium or 304 stainless steel in comparison with blue laser microjoining of T2 copper.

Discussion

In blue laser microjoining of thin materials, the viscous resistant stress, buoyant force, and surface tension pressure had a minor influence on the thin molten pools convection and stability. Marangoni stress affected the convective patterns and promoted melt-through of the thin molten pool. As shown in Fig. 11, in blue laser microjoining of copper, the molten temperature gradient was low and the surface tension gradient was negative; Marangoni stress was low and the molten metal flowed outward at both the top and bottom surfaces; inside the molten pool, the molten metal flowed from the pool edge to the pool center (return flow). As a result, the molten pool surface deformed slightly, and the molten pool was stable. In blue laser microjoining of pure titanium, the molten temperature gradient was high and the surface tension gradient was negative; Marangoni stress was high, and the molten metal flowed backward strongly from the pool center to the pool edge while the return flow in the trailing part of the molten pool was weak. As a result, the molten pool became thinner and melt-through occurred. In blue laser microjoining of 304 stainless steel, the molten temperature gradient was high and the surface tension gradient was positive; the molten metal flowed inward at both the top and bottom surfaces at the beginning. With time, the molten pool size increased, and the molten metal flowed backward strongly from the pool center to the pool edge, causing serious deformation of the molten pool. The return flow in the trailing part of the molten pool was weak, and melt-through occurred.

The Peclet number (Pe) and Marangoni number (Ma) of the thin molten pool are calculated (Ref. 29):

$$\mathrm{Pe} = \frac{\rho U L c_p}{k} \tag{13}$$

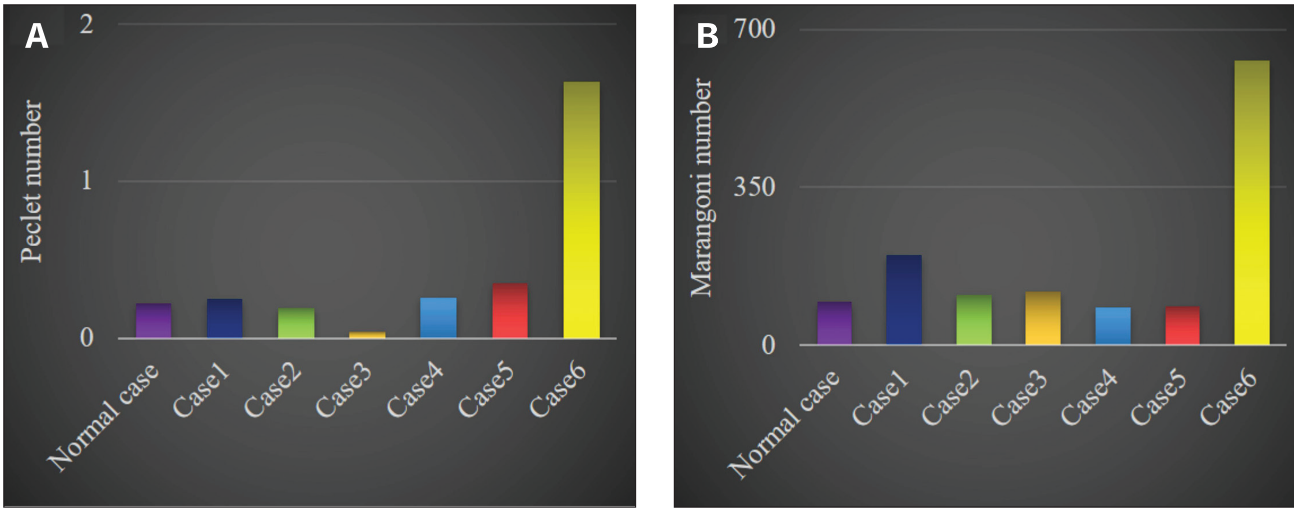

Fig. 12 — Peclet and Marangoni numbers in different cases: A — Peclet number; B — Marangoni number.

$$\mathrm{Ma} = \frac{-\frac{\partial \gamma}{\partial T}(\Delta T)\rho L c_p}{\mu k} \quad (14)$$

where U is maximum molten velocity, L is the radius of the molten pool surface, c_p is the specific heat, and ΔT is the temperature difference between the center and edge of the pool surface.

The density, specific heat, and thermal conductivity were calculated at the average value of the maximum molten temperature. In blue laser microjoining of T2 copper, the average values of the maximum molten velocity and surface tension gradient were used. The Peclet and Marangoni numbers in seven cases are shown in Fig. 12. As the Peclet number is a dimensionless number showing the ratio between convection and conduction (Ref. 29), heat transfer is seen to be dominated by conduction at low values of the Peclet number. The Marangoni number is a measure of the extent of Marangoni convection. In the normal case, the Peclet number was only 0.22, so heat conduction dominated; the Marangoni number was 96.7. With half viscosity (Case 1), half surface tension (Case 2), zero surface tension gradient (Case 3), double surface tension gradient (Case 4), or positive surface tension gradient (Case 5), the Peclet number and Marangoni number of the molten pool did not change significantly. With half thermal conductivity (Case 6), the maximum molten temperature and temperature gradient increased, as did the molten pool size and molten velocity; the Peclet and Marangoni numbers of the molten pool increased to 1.63 and 630.2, respectively; the Marangoni convection became strong and melt-through of the thin molten pool occurred.

Compared with T2 copper, pure titanium has lower viscosity and thermal conductivity and higher surface tension. In blue laser microjoining of pure titanium, the Peclet and Marangoni numbers of the molten pool before the melt-through are 14.16 and 4943.9, respectively. The 304 stainless steel has lower thermal conductivity and higher viscosity and surface tension. In blue laser microjoining of 304 stainless steel, the Peclet and Marangoni numbers of the molten pool are 21.05 and 3896.7, respectively. The Marangoni convection dominates and Marangoni stress is the main driving force for the instability of the thin molten pool.

During the manufacturing of electric vehicles, the microjoining of thin materials, such as copper, stainless steel, and aluminum, is necessary. The material properties have great influences on the stability of the thin molten pool. Based on the numerical simulation and experiment, it can be concluded that the thin molten pool is stable with low Peclet and Marangoni numbers.

Conclusion

A blue laser was adopted to realize the microjoining of a copper material with a thickness of 0.1 mm, and the dynamic behaviors of the molten pool were studied. The following conclusions were drawn:

A thin molten pool with a very low molten height-to-length ratio was formed. At both the top and bottom surfaces, the liquid metal flowed outward from the pool center to the pool edge under the driving of Marangoni stress.

Marangoni stress promoted melt-through of the thin molten pool, while the viscous resistant stress, buoyant force, and surface tension pressure had minor influences on it.

The Peclet and Marangoni numbers can be used to predict the stability of the thin molten pool. With low Peclet and Marangoni numbers, heat conduction dominates and the thin molten pool is stable.

Acknowledgments

This research was partially supported by funding from the National Natural Science Foundation of China (No. 52101044) and the Sichuan Science and Technology Program (2022JDRC0071).

References

1. Saariluoma, H., Piiroinen, A., Unt, A., Hakanen, J., Rautava, T., and Salminen, A. 2020. Overview of optical digital measuring challenges and technologies in laser welded components in EV battery module

design and manufacturing. *Batteries* 6(3): 47–62. DOI: 10.3390/batteries6030047

2. Ramesh, P., and Lenin, N. C. 2019. High power density electrical machines for electric vehicles — Comprehensive review based on material technology. *IEEE Transactions on Magnetics* 55(11): 1–21. DOI: 10.1109/TMAG.2019.2929145

3. Das, A., Li, D. Z., Williams, D., and Greenwood, D. 2019. Weldability and shear strength feasibility study for automotive electric vehicle battery tab interconnects. *Journal of the Brazilian Society of Mechanical Sciences and Engineering* 41(1): 54–68. DOI: 10.1007/s40430-018-1542-5

4. Cho, W. I., and Woizeschke, P. 2021. Analysis of molten pool dynamics in laser welding with beam oscillation and filler wire feeding. *International Journal of Heat and Mass Transfer* 164: 120623. DOI: 10.1016/j.ijheatmasstransfer.2020.120623

5. Ono, K., Sato, Y., Higashino, R., Funada, Y., Abe, N., and Tsukamoto, M. 2021. Pure copper rod formation by multibeam laser metal deposition method with blue diode lasers. *Journal of Laser Applications* 33(1): 012013. DOI: 10.2351/7.0000322

6. Maina, M. R., Okamoto, Y., Hamada, K., Okada, A., Nakashiba, S. I., and Nishi, N. 2022. Effects of superposition of 532 nm and 1064 nm wavelengths in copper micro-welding by pulsed Nd: YAG laser. *Journal of Materials Processing Technology* 299: 117388. DOI: 10.1016/j.jmatprotec.2021.117388

7. Ning, J., Zhang, L. J., Yin, X. Q., Zhang, J. X., and Na, S. J. 2019. Mechanism study on the effects of power modulation on energy coupling efficiency in infrared laser welding of highly-reflective materials. *Materials & Design* 178: 107871. DOI: 10.1016/j.matdes.2019.107871

8. Franco, D., Oliveira, J. P., Santos, T. G., and Miranda, R. M. 2021. Analysis of copper sheets welded by fiber laser with beam oscillation. *Optics & Laser Technology* 133: 106563. DOI: 10.1016/j.optlastec.2020.106563

9. Dadras, S., Torkamany, M. J., and Sabbaghzadeh, J. 2008. Spectroscopic characterization of low-nickel copper welding with pulsed Nd: YAG laser. *Optics and Lasers in Engineering* 46(10): 769-776. DOI: 10.1016/j.optlaseng.2008.04.023

10. Yang, H., Tang, X. H., Hu, C., Liu, S. J., Fan, Y. C., Xiao, Y., Lu, G. J., Wang, Q., Chen, G. N., Xing, P. Y., Tan, H., Guo, Z. X., and Niu, Z. Q. 2021. Study on laser welding of copper material by hybrid light source of blue diode laser and fiber laser. *Journal of Laser Applications* 33(3): 032018. DOI: 10.2351/7.0000386

11. Fujio, S., Sato, Y., Takenaka, K., Ito, R., Ito, M., Harada, M., and Tsukamoto, M. 2021. Welding of pure copper wires using a hybrid laser system with a blue diode laser and a single-mode fiber laser. *Journal of Laser Applications* 33(4): 042056. DOI: 10.2351/7.0000502

12. Hummel, M., Schöler, C., Häusler, A., Gillner, A., and Poprawe, R. 2020. New approaches on laser micro welding of copper by using a laser beam source with a wavelength of 450 nm. *Journal of Advanced Joining Processes* 1: 100012. DOI: 10.1016/j.jajp.2020.100012

13. Britten, S., and Krause, V. 2019. Industrial blue diode laser breaks 1 kW barrier. *PhotonicsViews* 16(2): 30–33. DOI: 10.1002/phvs.201900017

14. Morimoto, K., Tsukamoto, M., Masuno, S., Azumi, K., Hayafshi, Y., and Abe, N. 2019. Influence of laser wavelength on melt pool behavior in welding of thin pure copper plate with blue diode and fiber lasers. *Lasers in Manufacturing Conference*., pp. 1–5. RWTH Aachen Univ. Press.

15. Zediker, M. S., Fritz, R. D., Finuf, M. J., and Pelaprat, J. M. 2019. Stable keyhole welding of 1 mm thick copper with a 600 W blue laser system. *Journal of Laser Applications* 31(2): 022404. DOI: 10.2351/1.5096092

16. Pelaprat, J. M., Finuf, M., Fritz, R., and Zediker, M. 2018. Seeing things in a new light: High power blue lasers for metal processing. *Laser Technik Journal* 15(4): 39–41. DOI: 10.1002/latj.201800028

17. Zediker, M. S., Fritz, R. D., Finuf, M. J., and Pelaprat, J. M. 2020. Laser welding components for electric vehicles with a high-power blue laser system. *Journal of Laser Applications* 32(2): 022038. DOI: 10.2351/7.0000054

18. Mills, K. C. 2002. *Recommended Values of Thermophysical Properties for Selected Commercial Alloys*. Cambridge, England: Woodhead Publishing.

19. Cho, J. H., and Na, S. J. 2009. Three-dimensional analysis of molten pool in GMA-laser hybrid welding. *Welding Journal* 88(2): 35-s to 43-s.

20. Cho, M. H., Lim, Y. C., and Farson, D. F. 2006. Simulation of weld pool dynamics in the stationary pulsed gas metal arc welding process and final weld shape. *Welding Journal* 85(12): 271-s.

21. Bayon, A., Toro, J. P., Bombardelli, F. A., Matos, J., and López-Jiménez, P. A. 2018. Influence of VOF technique, turbulence model and discretization scheme on the numerical simulation of the non-aerated, skimming flow in stepped spillways. *Journal of Hydro-environment Research* 19: 137–149. DOI: 10.1016/j.jher.2017.10.002

22. Wang, H. Z., Wu, Y., and Wang, H. W. 2021. Current status of applying blue laser in nonferrous metals processing. *The Chinese Journal of Nonferrous Metals* 31(11): 3059–3070. DOI: 10.11817/j.ysxb.1004.0609. 2021-42030

23. Wang, H., Kawahito, Y., Yoshida, R., Nakashima, Y., and Shiokawa, K. 2018. A model to calculate the laser absorption property of actual surface. *International Journal of Heat and Mass Transfer* 118: 562–569. DOI: 10.1016/j.ijheatmasstransfer.2017.11.023

24. Wu, D. S., Hua, X. M., Li, F., and Huang, L. J. 2017. Understanding of spatter formation in fiber laser welding of 5083 aluminum alloy. *International Journal of Heat and Mass Transfer* 113: 730–740. DOI: 10.1016/j.ijheatmasstransfer.2017.05.125

25. Mills, K. C., and Brooks, R. F. 1994. Measurements of thermophysical properties in high temperature melts. *Materials Science and Engineering A* 178: 77–81. DOI: 10.1016/0921-5093(94)90522-3

26. Kou, S., Limmaneevichitr, C., and Wei, P. S. 2011. Oscillatory Marangoni flow: a fundamental study by conduction-mode laser spot welding. *Welding Journal* 90(12): 229-s to 240-s.

27. Lee, J. Y., Ko, S. H., Farson, D. F., and Yoo, C. D. 2002. Mechanism of keyhole formation and stability in stationary laser welding. *Journal of Physics D: Applied Physics* 35(13): 1570. DOI: 10.1088/0022-3727/35/13/320

28. Huang, L. J., Hua, X. M., Wu, D. S., and Li, F. 2018. Numerical study of keyhole instability and porosity formation mechanism in laser welding of aluminum alloy and steel. *Journal of Materials Processing Technology* 252: 421–431. DOI: 10.1016/j.jmatprotec.2017.10.011

29. Limmaneevichitr, C., and Kou, S. 2000. Experiments to simulate effect of Marangoni convection on weld pool shape. *Welding Journal* 79(8): 231-s to 237-s.

DONGSHENG WU, **JUNHAO SUN** (*1392672372sjh@sjtu.edu.cn*), **ZHUGUO LI**, **JIAN HUANG**, and **KE FENG** are with Shanghai Key Laboratory of Material Laser Processing and Modification, Shanghai Jiao Tong University, Shanghai, China. **WU** is also with the School of Electromechanical Engineering, Guangdong University of Technology, Guangzhou, China. **SUN**, **LI**, and **FENG** are also with Yibin Innovation Center for Advanced Materials, Yibin, China.